Atomic cation-vacancy modulated peroxymonosulfate nonradical oxidation of sulfamethoxazole via high-valent iron-oxo species

Xiaoyue Zhou [a], Renli Yin [a,*], Jieqiong Kang [a], Zhenjie Li [a], Yanan Pan [a], Jieyun Bai [b], Adela Jing Li [a,*], Rongliang Qiu [a]

[a] *Guangdong Laboratory for Lingnan Modern Agriculture, Guangdong Provincial Key Laboratory of Agricultural & Rural Pollution Abatement and Environmental Safety, College of Natural Resources and Environment, South China Agricultural University, Guangzhou 510642, China*
[b] *College of Information Science and Technology, Jinan University, Guangzhou, China*

ARTICLE INFO

ABSTRACT

The formation of high-valent active species during peroxymonosulfate (PMS) activation has attracted great interest. However, how to rapidly generate high-valent active species during PMS activation process remains ambiguous. Herein, iron vacancy anchored layered double hydroxides activated PMS process were designed to enhance the removal rate of sulfamethoxazole (SMX) by 30.0 times to PMS alone, which even showed much superiority to the homogeneous Fe^{2+}/PMS system. Due to the cooperation of Fe vacancies, PMS favored to be adsorbed on Fe2 sites (adjacent to iron vacancy) and combined with Fe2 sites to form Fe(II)-O-SO_3-OH complex. Then, the accepted electrons led to the cleavage of S-O bond in Fe(II)-O-SO_3-OH complex, resulting in the spontaneous generation of $Fe^{(IV)}$=O/$Fe^{(V)}$=O species. Finally, PMS activation pathways were proposed from radical oxidation to nonradical oxidation via high-valent iron-oxo species. This study provides a new perspective on generation of high-valent iron-oxo species for excellent performance and resistance with real wastewater.

1. Introduction

Advanced oxidation processes (AOPs) based on peroxymonosulfate (PMS), which can produce various types of highly active radicals to decompose and even mineralize organics, have received growing interest in the decontamination of organic pollutants from water [1–3]. Transition metals are generally regarded as the promising activators owing to the advantages of high efficiency, easy operation and low energy consumption [4–6]. For instance, typical Fe^{2+}/PMS system showed excellent degradation properties for organic pollutants with consecutive production of sulfate radicals [7]. However, the slow reduction of Fe(III) to Fe(II) greatly hindered the efficiency of electron transfer coupled with the formation of iron oxyhydroxide sludge that restrained PMS activation [7,8].

Formation of high-valent iron-oxo species is a new avenue for wastewater remediation via nonradical oxidation pathways of PMS activation due to its high redox potential, long half-life and selective reaction [9,10]. Bao et al. [11] proposed the way for generating ≡Fe^{IV}=O in activating PMS on the surface of Zn-Fe layered double hydroxide (Zn-Fe-LDH) by using zinc hydroxide, which could function

over a wide pH range (3.0–11.0) for wastewater treatment practices. However, it remains challenging to rationally design highly efficient and selective catalysts to tune PMS activation for rapidly generating high-valent active species for pollutant removal.

Defects engineering has been rationally imported as an effective way to modulate electronic properties of materials with continuous electron-transfer ability during PMS activation [12–15]. Significantly, it is possible to change the activation pathway of PMS to generate high-valent active species by introducing vacancies. Jiang et al. [16], reported that nitrogen vacancies modulated the major active species of PMS from $^1O_2$ to high-valent colbalt-oxo species. Yu et al. [17], developed an oxygen-vacancy-enriched WO_{3-x} to shift the reaction of Fe^{II} with H_2O_2 from the formation of Fe^{III} towards the direct generation of Fe^{IV}. These anionic vacancies derived from nitrogen or oxygen was built on materials to improve catalytic performance for PMS activation through the enhancement of charges transfer. On the contrary, cation vacancies, which could construct new metal active sites at second neighboring to the atomic vacancies, might provide larger potential for generating more high-valent active species [18,19]. To the best of our knowledge, little study worked on effect of cation vacancies for
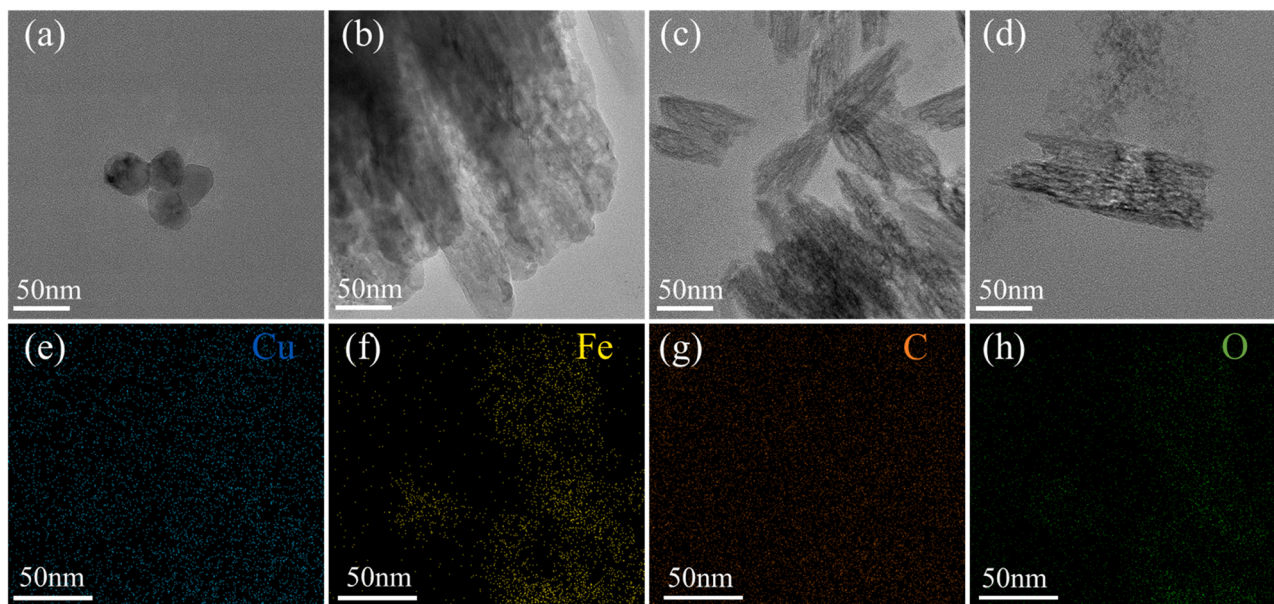

Fig. 1. TEM image for Cu-Fe-LDH (a), Cu^{vac}-Fe-LDH (b), Cu-Fe^{vac}-LDH (c), and Cu^{vac}-Fe^{vac}-LDH (d), and TEM energy dispersive X-ray (STEM-EDX) elemental mapping of Cu (e), Fe (f), C (g) and O (h) elements scanned separately for Cu-Fe^{vac}-LDH.

generation of high-valent active species during PMS activation and its efficiency in removal of organic contaminants.

Therefore, this study aims to uncover the effect of cation vacancies anchored on copper-iron layered double hydroxide (Cu-Fe-LDH) for PMS activation, particularly to make clear the generation mechanism of high-valent iron-oxo species. The cation vacancies-contained Cu-Fe-LDH was systematically investigated for its efficiency in degradation of sulfamethoxazole (SMX) through PMS activation. Theoretical calculations were further performed to reveal the mechanism on generation of high-valent iron-oxo species and the potential electron-transfer behavior in the system. The generation of high-valent active species in cation vacancies-induced PMS activation process may provide a new strategy for wastewater remediation.

2. Materials and methods

2.1. Chemicals and materials

Standards of PMS, 5,5-dimethyl-1-pyrroline-N-oxide (DMPO) and sulfamethoxazole (SMX) were obtained from Sigma-Aldrich. Methanol (MeOH), triacetonediamine (TEMP), furfuryl alcohol (FFA), methyl phenyl sulfoxide (PMSO), tert-butyl alcohol (TBA), benzoquinone (p-BQ) and urea (($NH_4)_2CO$) were obtained from Aladdin. Dimethyl sulfoxide (DMSO) was obtained from MP Biomedicals. Compounds of $CuCl_2\cdot2\ H_2O$, $FeCl_3\cdot3\ H_2O$, $AlCl_3\cdot6\ H_2O$, $ZnCl_2$, ethylene diamine tetraacetic acid (EDTA) and NaOH were purchased for Guangzhou Puzhi Ecological and Chemical Reagent Industry. All of the chemicals were at least analytic grade and used without further purification, unless specified otherwise. Ultra-pure water was prepared using a Milli-Q Integral system (Millipore, Molsheim, France).

2.2. Preparation of LDH catalysts

The method of catalyst synthesis referred to a previous study, using a typical hydrothermal reaction method [20]. Briefly, a homogeneous solution was prepared by dissolving 0.90 mmol $CuCl_2\cdot2\ H_2O$, 0.30 mmol $FeCl_3\cdot3\ H_2O$ and 7.0 mmol ($NH_4)_2CO$ in 30 mL ultra-pure water under constant magnetic stirring for 30 min. The resulting solution was transferred to a 50 mL Teflon-lined stainless steel autoclave and kept at 150 °C for 6 h. After cooling to room temperature naturally, the

Cu-Fe-LDH product was collected by centrifugation (5000 rpm, 5 min), washed three times alternately with ultra-pure water and absolute ethanol, and finally dried in an oven at 60 °C.

2.3. Synthesis of cation vacancy products

The vacancy products of Cu^{vac}-Fe-LDH, Cu-Fe^{vac}-LDH and Cu^{vac}-Fe^{vac}-LDH (where ^{vac} is a cation vacancy) were obtained from Cu-Fe-Zn-LDH, Cu-Fe-Al-LDH and Cu-Fe-Zn-Al-LDH, respectively. The synthesis of Cu-Fe-Zn-LDH, Cu-Fe-Al-LDH and Cu-Fe-Zn-Al-LDH were similar to that of Cu-Fe-LDH described above. The molar ratio of metal precursors was all fixed as 7: 3: 0.3 of Cu(II): Fe(III): Al(III) for Cu-Fe-Al-LDH, Cu(II): Fe(III): Zn(II) for Cu-Fe-Zn-LDH, and 7: 3: 0.3: 0.3 of Cu(II): Fe(III): Zn(II): Al(III) for Cu-Fe-Zn-Al-LDH. Following hydrothermal synthesis, the obtained metal precursors were soaked in 10 mL of 6.0 M NaOH solution at 60 °C for 3 h individually for removal of Zn(II) and Al(III) ions selectively. The vacancy products were collected and washed with ultra-pure water and ethanol three times. To completely remove the amphoteric Zn(II) and Al(III) ions in the LDH precursor, the alkalization step was repeated three times. The etched product was finally dried in an oven at 60 °C overnight for further use.

2.4. Experimental procedure

Degradation experiments were performed in a 30.0 mL reactor with magnetic stirring at 700 rpm at room temperature. Compounds with preset concentrations (such as SMX 10.0 mg L^{-1} and catalyst 0.10 g L^{-1}) were added to the reactor to form a 20.0 mL reaction system (pH = 5.0), and adsorbed for 30 min to reach the adsorption-dissociation equilibrium. Then, PMS at 0.10 g L^{-1} was added to the reactor to trigger the reaction. During the whole reactions, aliquots were periodically collected and filtered through 0.22 μm PTFE filters (ANPEL, China), and loaded into HPLC vials for immediate analysis. Compounds of MeOH, FFA, p-BQ, EDTA and DMSO were used to scavenge •OH, SO$_4^{\bullet-}$, $^1O_2$, O$_2^{\bullet-}$ and Fe$^{(IV)}$=O/Fe$^{(V)}$=O, respectively. PMSO was used to quantify the contribution of Fe$^{(IV)}$=O/Fe$^{(V)}$=O. Analytical methods of various LDH materials, SMX degradation products, PMS and some ions are detailed in Text S1-S2.
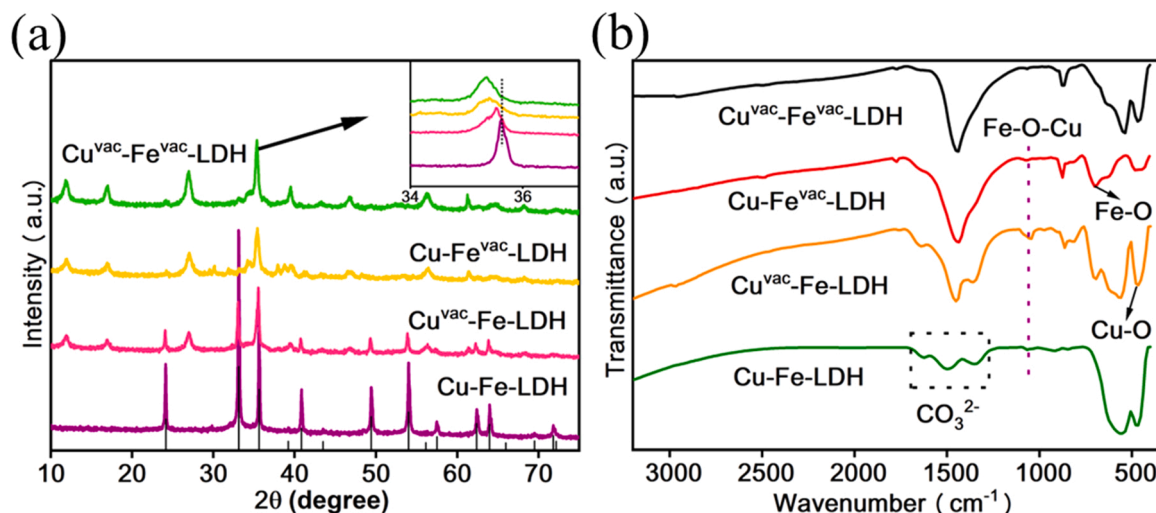
Fig. 2. XRD patterns (a) and FTIR spectra (b) of Cu-Fe-LDH, Cu^{vac}-Fe-LDH, Cu-Fe^{vac}-LDH and Cu^{vac}-Fe^{vac}-LDH.

2.5. Computational methods

All spin-polarized density generalized function theory (DFT) calculations was firstly estimated using the Vienna ab initio Simulation Package (VASP) with projector augmented ware (PAW). The Perdew-Burke-Ernzerhof (PBE) formulae with the latest dispersion correction (DFT-D2) and polarized spin was used to build exchange correlation functions. The energy cutoff was set to 400 eV and the Monkhorst-Pack K-point grid was set to $3 \times 3 \times 1$. The Gaussian electron smearing method was set at $\sigma = 0.05$ eV. The convergence condition of geometric optimization of the forces and energy tolerances was set at less than

0.05 eV/Å and 10^{-5} eV/atom, respectively.

3. Results and discussion

3.1. Characterization of catalysts

Images from scanning electron microscopy (SEM) (Fig. S1) showed that Cu-Fe-LDH, Cu^{vac}-Fe-LDH, Cu-Fe^{vac}-LDH and Cu^{vac}-Fe^{vac}-LDH all presented typical nanosheet structures, which were beneficial to full utilization of the active sites on the materials. The images from transmission electron microscopy (TEM) (Fig. 1a-d) and energy-dispersive X-
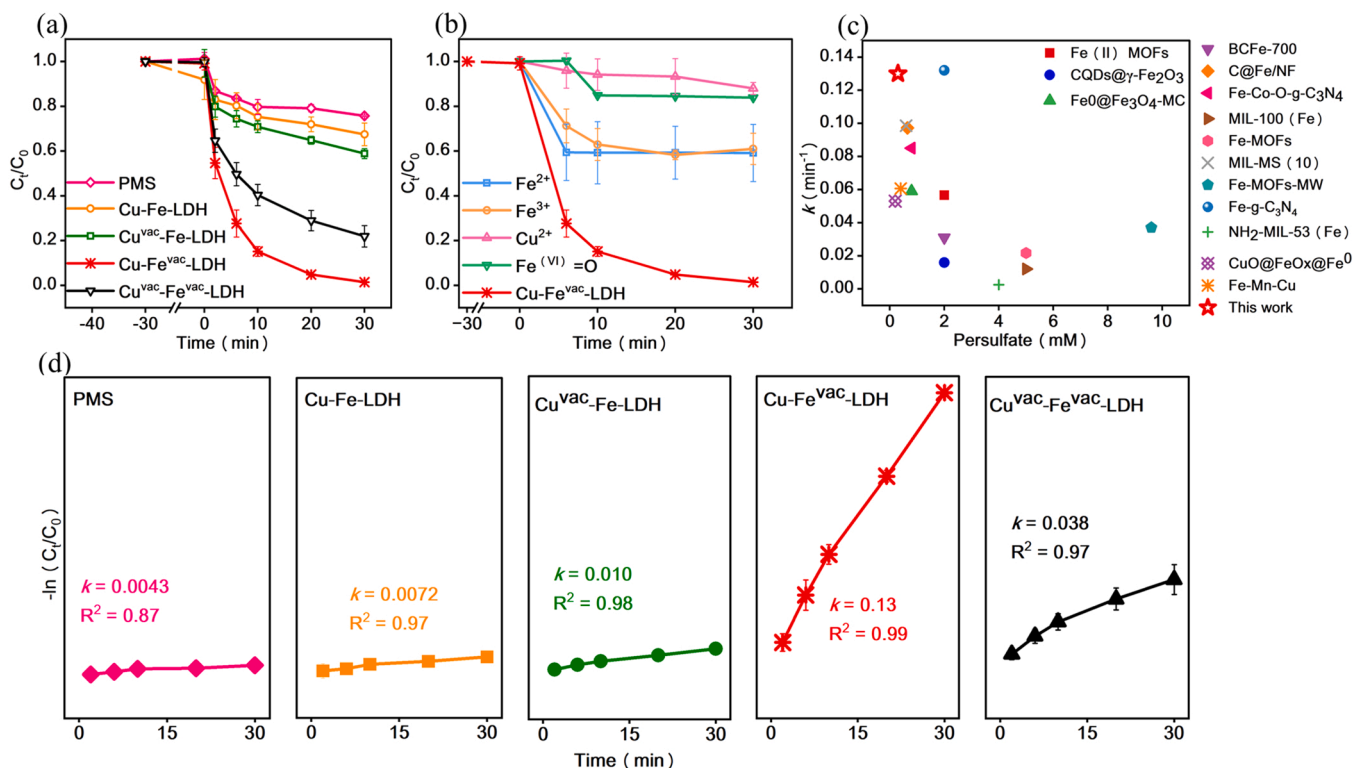

Fig. 3. SMX degradation under different oxidation processes (a), different homogeneous oxidation processes (b), comparison of the performance of Cu-Fe^{vac}-LDH/PMS process for catalytic degradation of SMX with previously reported iron-based catalyst/oxidant processes (c), and pseudo-first order kinetics of SMX degradation under different oxidation processes (d). Experimental conditions: (a): [SMX] = 10.0 mg L^{-1}, [PMS] = 0.10 g L^{-1}, [catalyst] = 0.10 g L^{-1} and pH = 5.0; (b) [Cu^{2+}] = [Fe^{2+}] = [Fe^{3+}] = [Fe$^{(VI)}$=O] = 0.30 mg L^{-1}, [SMX] = 10.0 mg L^{-1}, [PMS] = 0.10 g L^{-1} and pH = 5.0.
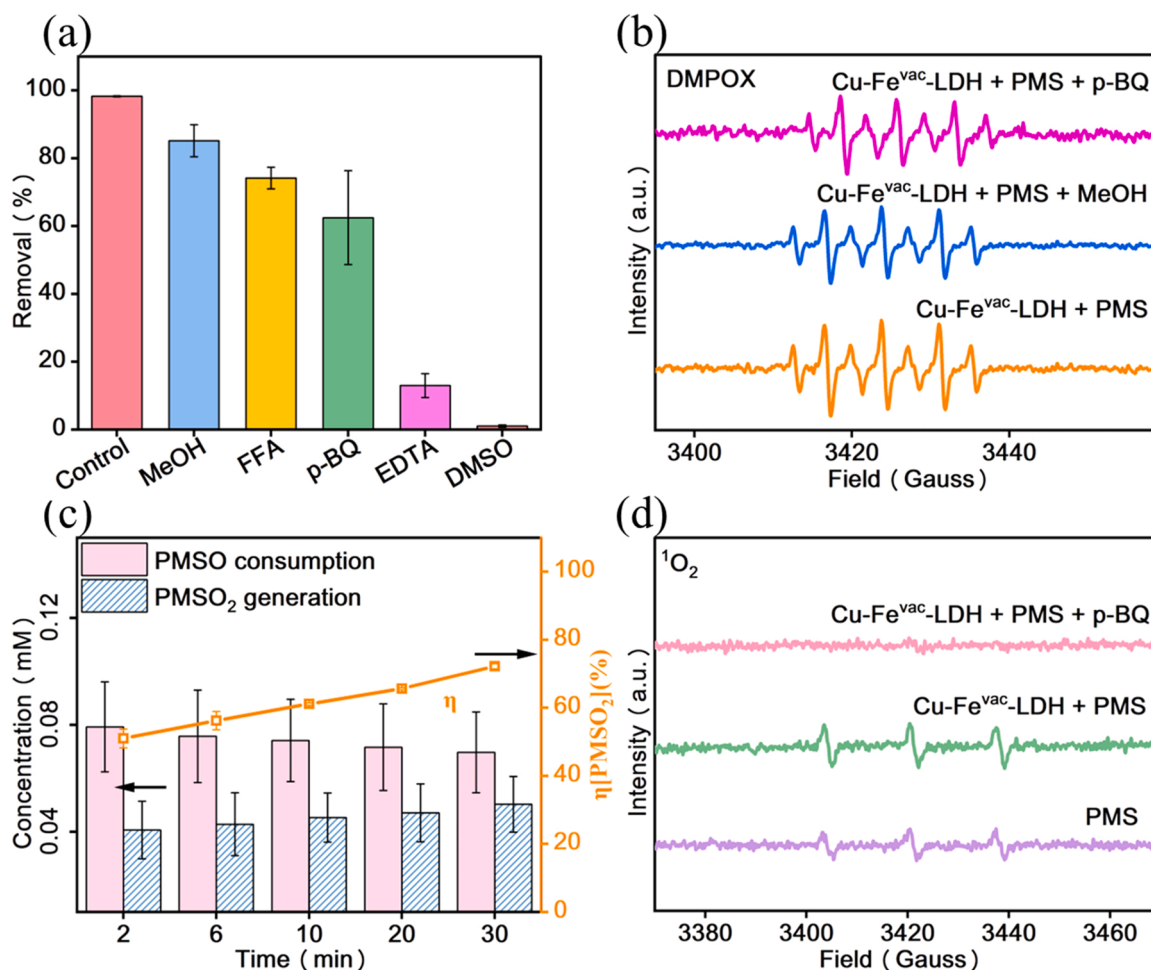
Fig. 4. The scavenging tests of Cu-Fe^{vac}-LDH/PMS process (a), EPR spectra of DMPO (b) and TEMP (d) for Cu-Fe^{vac}-LDH, PMSO consumption, PMSO$_2$ generation and the calculated η(PMSO$_2$) values of Cu-Fe^{vac}-LDH/PMS process (c). Experimental conditions: (a): [MeOH] = 40 mM, [FFA] = 40 mM, [p-BQ] = 2.0 mM, [EDTA] = 2.0 mM, [DMSO] = 0.10 M; (c): [PMSO] = 20.0 mg L^{-1}, [PMS] = 0.10 g L^{-1}, [catalyst] = 0.10 g L^{-1}, and pH = 5.0.

ray (EDX) elemental mapping (Fig. 1e-h) exhibited lattice fringe and uniform element distribution in the LDH nanosheets. The X-ray diffraction (XRD) pattern (Fig. 2a) showed that diffraction pattern of the LDH nanosheets was in good agreement with JCPDS no. 49-0929. Compared with Cu-Fe-LDH, after alkaline etching of LDH (Cu^{vac}-Fe-LDH, Cu-Fe^{vac}-LDH, Cu^{vac}-Fe^{vac}-LDH), the original peak (83) shifted to a lower 2θ angle. Moreover, the original peak intensity became weak and new peaks appeared during the etching process. The new peak grew gradually and coexisted with the original peak for a certain period of time. It indicated that the crystal plane of LDH nanosheets was changed through introducing the vacancies by alkali etching, which could ascribe to phase transition and interlayer space change by the enhanced repulsive force between the LDH substrates [20,21]. The Fourier transform infrared (FTIR) spectra of the synthesized LDHs were shown in Fig. 2b. The bands at 1043 cm^{-1} and 1344–1641 cm^{-1} were attributed to Fe-O-Cu and CO$_3^{2-}$, respectively [11,22], with enhanced peak intensities after alkali etching, indicating successful introduction of the vacancies in LDHs. The above characterization results showed that the successful introduction of vacancies had certain advantages compared with the initial structure, which might provide new potential and catalytic capacity on PMS activation for organics degradation.

3.2. Effects of cation vacancies on catalytic performance

The effects of cation vacancies on the catalytic performance of LDH were investigated. Relative to removal efficiency of SMX by pristine Cu-

Fe-LDH activated PMS (less than 30 % in 30 min), the introduction of Fe vacancies in Cu-Fe^{vac}-LDH and Cu^{vac}-Fe^{vac}-LDH activated PMS significantly enhanced SMX elimination at 98 % and 80 %, respectively (Fig. 3a). However, the introduction of Cu vacancies in LDH could not efficiently improve the catalytic capacity of LDH. The limited adsorption of SMX on LDHs (Fig. S2a) and improved PMS decomposition by LDHs (Fig. S2b) suggested a better performance of LDHs coupled PMS in the removal of SMX. In addition, for the apparent leaching metal ion concentration, which were below the emission standard of Fe^{2+}, Fe^{3+} (0.30 mg L^{-1}) and Cu^{2+} (1.0 mg L^{-1}) according to GB 8978-1996, showed insignificant effect for PMS activation in the removal of SMX (Fig. 3b). The degradation of SMX in the LDHs/PMS processes were mainly attributed to heterogeneous catalytic effects rather than homogeneous Fenton-like effects. Furthermore, the apparent rate constant (k, -ln(C/C$_0$) = kt) of Cu-Fe^{vac}-LDH/PMS process (0.13 min^{-1}) was approximately 30.0, 18.0, 13.0 and 3.4 times higher than these of PMS alone, Cu-Fe-LDH, Cu^{vac}-Fe-LDH and Cu^{vac}-Fe^{vac}-LDH activated PMS processes, respectively (Fig. 3d). It was obvious that the enhanced catalytic performance of LDHs was largely attributed to the introduction of Fe vacancies rather than Cu vacancies. And the Fenton-like performance of Cu-Fe^{vac}-LDH outperformed most state-of-the-art heterogeneous catalysts (Fig. 3c and Table S2). The decreased removal rate of SMX by Cu^{vac}-Fe^{vac}-LDH relative to Cu-Fe^{vac}-LDH has been verified that the introduction of Cu vacancies occupied the chemical sites and thus reduced the number of Fe vacancies in total (Table S3).
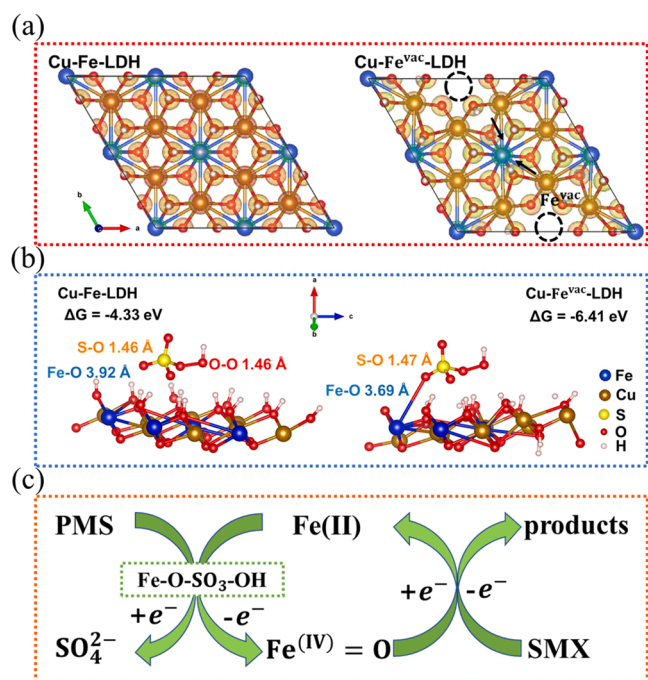
Fig. 5. Charge density difference of Cu-Fe-LDH and Cu-Fe^{vac}-LDH catalyst (a), adsorption configuration of PMS absorbed on Cu-Fe-LDH and Cu-Fe^{vac}-LDH catalyst (b), and the possible oxidation mechanism of SMX by Cu-Fe^{vac}-LDH/ PMS process (c).

3.3. Mechanistic effects of Fe vacancies on PMS activation

Radical scavenger experiments were further employed to study what kinds of reactive oxidative species played the role in the performance of Fe vacancies for PMS activation. The results showed that $SO_4^{\bullet-}$, $^{\bullet}OH$, $O_2^{\bullet-}$ and $^1O_2$ were not the major oxidative species in the Cu-Fe^{vac}-LDH/PMS process to degrade SMX when taking MeOH, FFA and p-BQ as the scavengers (Fig. 4a) [23–27]. It turned out that metal ions contributed a lot to SMX degradation, which was tested by scavenging effect of EDTA (i.e., a chelating agent for metal ions) [28,29]. The Fe^{2+}, Fe^{3+} and Cu^{2+} leached in this study have been verified to have limited effect on SMX removal (Fig. 3b). High-valent iron-oxo reactive species was speculated to be the key factor for SMX degradation because $Fe^{(IV)}=O$ and $Fe^{(V)}=O$ have been reported their significance in AOPs [30,31].

Furthermore, as shown in Fig. 4b, a set of signals with seven strong peaks ascribed to 5,5-dimethyl-2-oxo-pyrroline-1-oxyl (DMPOX) rather than DMPO-$SO_4^{\bullet-}$ or DMPO-$\bullet$OH adducts were observed in Cu-Fe^{vac}-LDH/PMS process [32]. Previous studies have confirmed that DMPO could be oxidized to DMPOX by free radicals (i.e., $SO_4^{\bullet-}$ and $\bullet$OH) and/or nonradicals (high-valent iron-oxo species or $^1O_2$) [33–36]. By taking MeOH or p-BQ as scavengers, the electron paramagnetic resonance (EPR) signal showed that contributions of $SO_4^{\bullet-}$, $\bullet$OH and $O_2^{\bullet-}$ to DMPOX production were limited. Although a typical 3-fold characteristic peak of TEMP-$^1O_2$ adduct was detected in the Cu-Fe^{vac}-LDH/PMS process, it disappeared at the presence of p-BQ in the process (Fig. 4d). This suggested that $^1O_2$ produced might be responsible for $O_2^{\bullet-}$ transformation rather than direct effect of Cu-Fe^{vac}-LDH/PMS process. Thus, high-valent iron-oxo species was exclusively a concern for the generation of DMPOX during Cu-Fe^{vac}-LDH/PMS process.

Inspired by previous work, when DMSO, a quencher for possible generation of high-valent iron-oxo species, was introduced to the Cu-Fe^{vac}-LDH/PMS process, the SMX degradation was completely stagnated (Fig. 4a) [37,38]. Moreover, PMSO was further adopted as a chemical probe because it could react with high-valent iron-oxo species to generate $PMSO_2$ but with free radicals to generate biphenyl products [30,39,40]. As shown in Fig. 4c, the formation of $PMSO_2$ was quantified,

where 0.074 mM of PMSO was consumed and 0.054 mM of $PMSO_2$ was produced after 30 min in the Cu-Fe^{vac}-LDH/PMS process. The yield of $PMSO_2$ ($\eta(PMSO_2)$), i.e., the molar ratio of produced $PMSO_2$ toward lost PMSO, was achieved 72.9 % throughout the oxidation process. It is noted that $Fe^{(IV)}=O$, $Fe^{(V)}=O$ and $Fe^{(VI)}=O$ can all oxidize PMSO to $PMSO_2$ via oxygen atom transfer [41,42]. The generation of $Fe^{(VI)}=O$ (0.30 mg L^{-1}) in this process was too low to exert efficiency in SMX degradation (Fig. 3b), inferring the SMX degradation in the Cu-Fe^{vac}-LDH/PMS process was manipulated by $Fe^{(IV)}=O/Fe^{(V)}=O$ species. Results from radical quenching and EPR signal in the Cu-Fe-LDH, Cu^{vac}-Fe-LDH and Cu^{vac}-Fe^{vac}-LDH/PMS were also investigated (Figs. S3–S5) and discussed (Text S3). In summary, the introduction of Fe vacancies to LDH could change PMS activation from the free radical pathway to nonradical-based pathway by the formation of high-valent iron-oxo species of $Fe^{(IV)}=O/Fe^{(V)}=O$ and thus enhance efficacy in pollutant degradation.

3.4. Mechanism of high-valent iron-oxo species generated by Fe vacancies

DFT calculation was performed to figure out how Fe vacancies regulated production of high-valent iron-oxo during the Cu-Fe^{vac}-LDH activation of PMS. Compared with the original Cu-Fe-LDH, distribution of electron cloud of Cu-Fe^{vac}-LDH was mostly concentrated in the Fe2 sites along with introduction of Fe vacancies, suggesting generation of new active sites (Fig. 5a). Moreover, molecular potential energy of Cu-Fe^{vac}-LDH (-413.5 eV) was higher than Cu-Fe-LDH (-426.7 eV) and Cu^{vac}-Fe-LDH (-420.6 eV) (Fig. S6), noting much more active property of Cu-Fe^{vac}-LDH. Further observations showed that PMS was more easily to be adsorbed at Fe2 sites of Cu-Fe^{vac}-LDH (lower Gibbs Free energy; Fig. 5b) with further formation of Fe(II)-O-SO_3-OH complexes (being confirmed by in-situ FTIR analysis; Fig. 6c). Compared with Cu-Fe-LDH/PMS process, a peak at 1117 cm^{-1} (the S-O bond of PMS) [16] shifted to 1134 cm^{-1} and consequently derived a new peak at 1188 cm^{-1} under Cu-Fe^{vac}-LDH/PMS process (Fig. 6c). This was probably due to the intrinsic relevance of Fe vacancies that Fe2 active sites could promote the adsorption of PMS and form Fe(II)-O-SO_3-OH complexes instead of directly breaking O-O bond to generate $SO_4^{\bullet-}$ as in Cu-Fe-LDH/PMS process. In addition, the shortened Fe-O bond (3.69 Å) and elongated S-O bond (1.47 Å) implied instability of the Fe(II)-O-SO_3-OH complex and favored production of high-valent iron-oxo species by cleaving to S-O bond in the Cu-Fe^{vac}-LDH/PMS process (Fig. 5b). Overall, the reaction mechanism of Fe(II) with $Fe^{(IV)}=O/Fe^{(V)}=O$ could be deduced as follows (Fig. 5c). PMS was firstly adsorbed on the catalyst surface and acted as an electron acceptor with aid of Fe2 site, which led to activation and splitting of S-O bond in the Fe(II)-O-SO_3-OH complex with spontaneous generation of $Fe^{(IV)}=O/Fe^{(V)}=O$ species. The excited state of $Fe^{(IV)}=O/Fe^{(V)}=O$ eventually returned to the ground states of Fe(III) and Fe(II), which was due to Fe vacancies promoting electron transfer in the next cycle, as evidenced by the enhanced Fe(II) ratio in Fe XPS spectra (Fig. 6a and b).

It is known that high-valent iron-oxo species can function well in the neutral and alkaline conditions [43]. At the optimum pH of 3.0 for Fenton reaction, SMX degradation under Cu-Fe^{vac}-LDH/PMS process dropped significantly to 30 % relative to pH of 5.0 (Fig. 7a). This could be explained that Cu-Fe^{vac}-LDH/PMS system did not rely on free radicals produced from Fenton-like reaction, and acting factor of $Fe^{(IV)}=O/Fe^{(V)}=O$ would undergo self-decomposition at lower pH levels [44,45]. On the other hand, SMX degradation could reach over 98 % at pH of 5.0–9.0, respectively, which were the optimum conditions for function of high-valent iron-oxo species [46]. The results underlined the significant role and advantages of high-valent iron-oxo species in Cu-Fe^{vac}-LDH/PMS process, and implied their potential application in practical wastewater treatment. Based on this, five types of wastewaters were introduced to test the performance of Cu-Fe^{vac}-LDH/PMS process for the removal of contaminants in real water bodies, including reservoir water (RW), lake water (LW), domestic sewage water (DSW), livestock
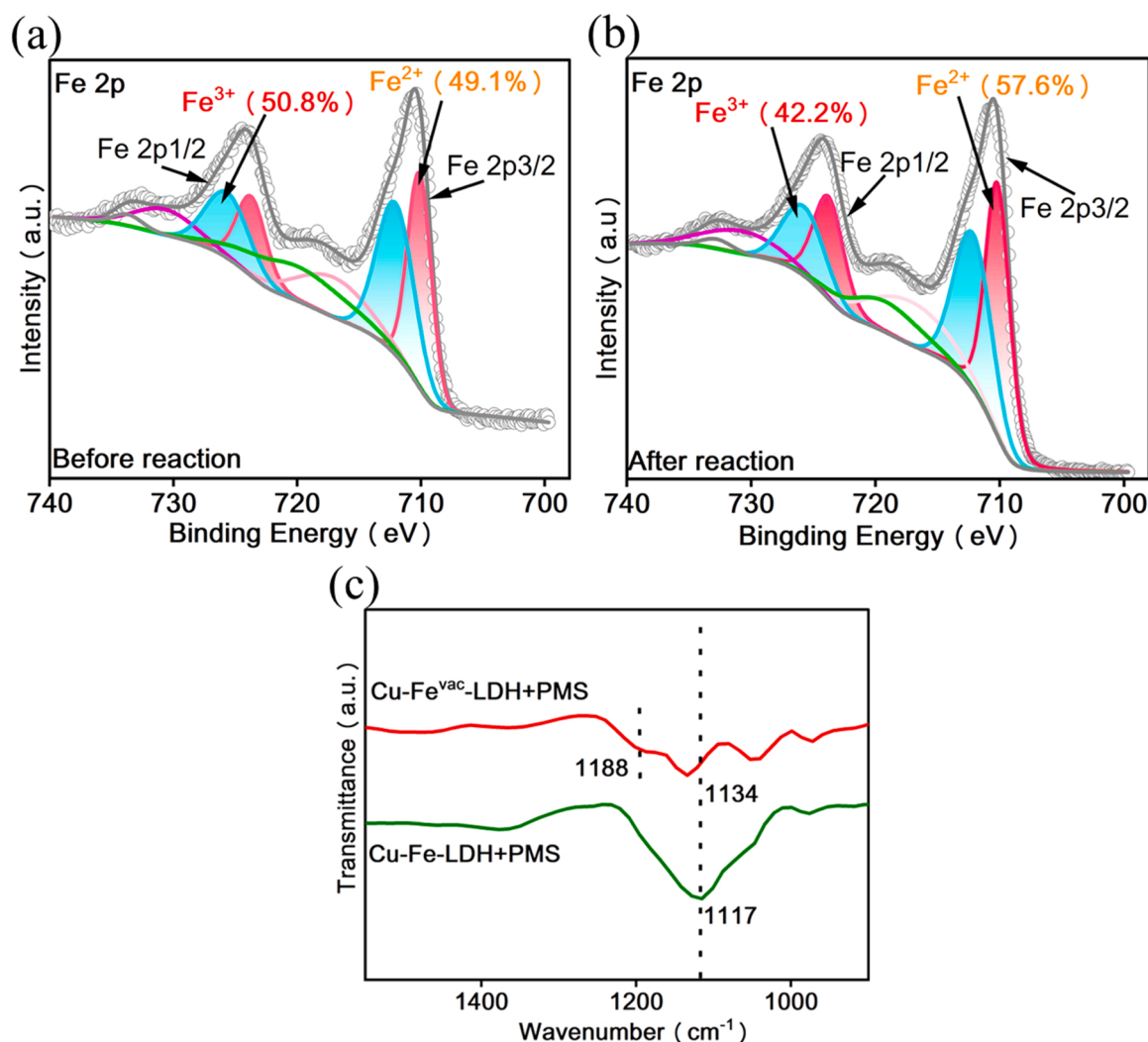
Fig. 6. Fe 2p spectra of before reaction (a) and after reaction (b) of Cu-Fe^{vac}-LDH, and in-situ FTIR spectrum of Cu-Fe-LDH and Cu-Fe^{vac}-LDH (c).
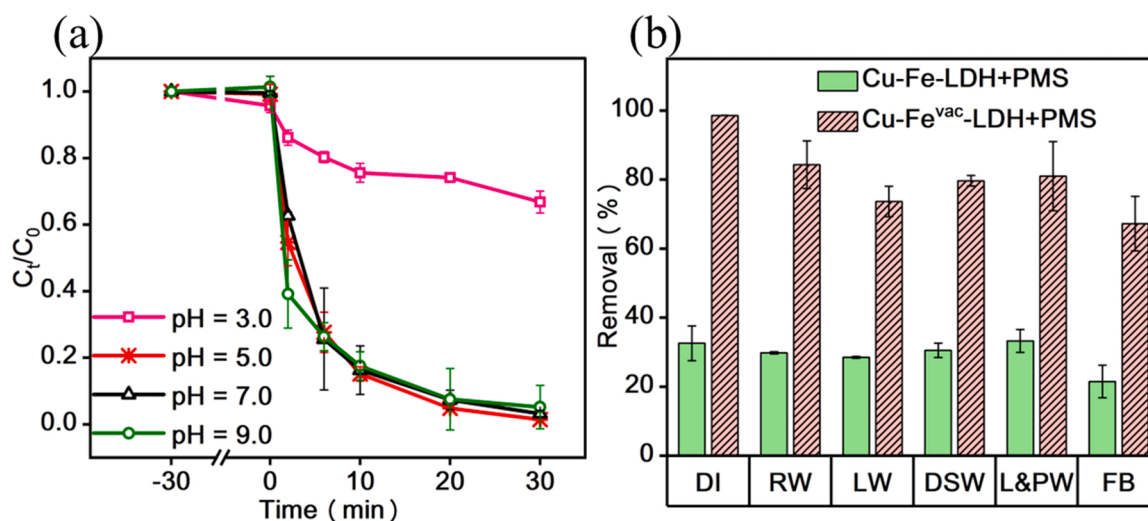

Fig. 7. Effects of initial pH concentration of Cu-Fe^{vac}-LDH/PMS process (a), degradation of SMX by Cu-Fe-LDH/PMS process and Cu-Fe^{vac}-LDH/PMS process under different real water systems (b). Experimental conditions: (a): [catalyst] = 0.10 g L^{-1}, [PMS] = 0.10 g L^{-1}, [SMX] = 10.0 mg L^{-1}; (b): [SMX] = 10.0 mg L^{-1}, [PMS] = 0.10 g L^{-1}, [catalyst] = 0.10 g L^{-1}.
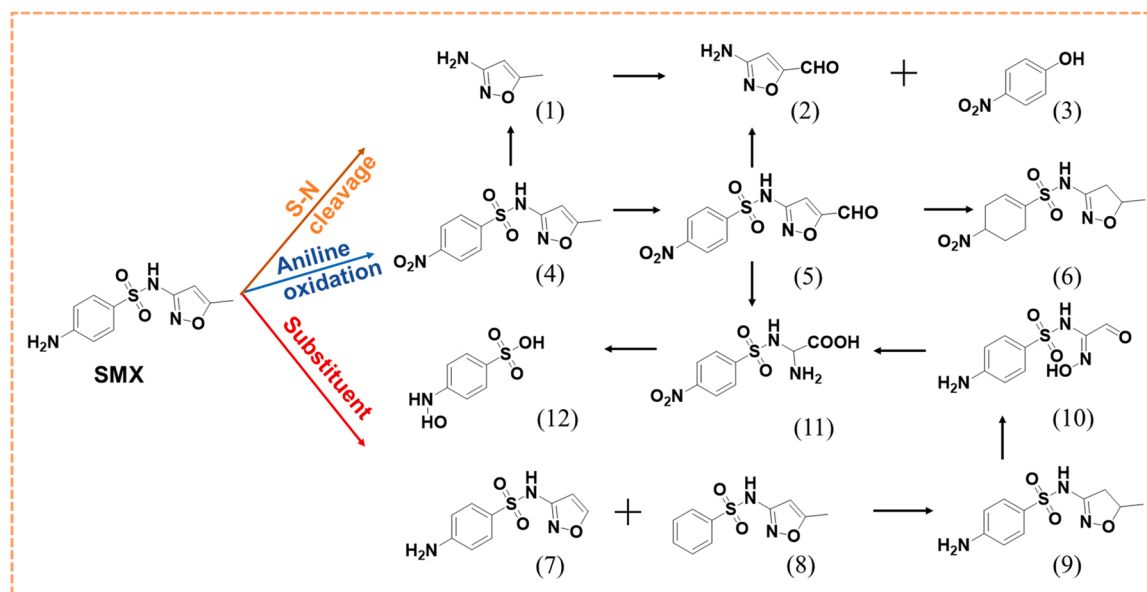
Fig. 8. Possible degradation pathways of SMX with Cu-Fe^{vac}-LDH/PMS process.

Fig. 9. Acute toxicity, bioconcentration factor, developmental toxicity, and mutagenicity of SMX and degradation intermediates.

and poultry wastewater (L&PW) and farm biogas (FB). The results showed that even though the real wastewater condition showed some effect on SMX degradation, SMX could be largely removed with the removal efficiency of 70–85 % (Fig. 7b). Thus, the Cu-Fe^{vac}-LDH/PMS process could function well in a wide pH range and real wastewater condition, suggesting that high-valent iron-oxo species performed high potential for eliminating SMX or other organics in the actual water matrix.

The presumed chemical structures of intermediate products and major degradation pathways of SMX in the Cu-Fe^{vac}-LDH/PMS process are illustrated in Fig. 8. The degradation pathways of SMX were proposed to include S-N bond cleavage, aniline oxidation and substitution. (1) S-N bond from SMX was proposed to be attacked and induced the formation of P1 ($m/z = 98$); (2) Product P4 ($m/z = 283$) formed by the oxidation of the aniline group; and (3) the oxazole ring occurred

addition and cleavage and formed the products P7 ($m/z = 239$), and P8 ($m/z = 238$). These products then underwent further redox reactions to produce a series of small molecules. Besides, the details of by-products were presented in Table S4.

To clear the safety of the Cu-Fe^{vac}-LDH/PMS process for SMX degradation, the acute toxicity (Daphnia magna), bioaccumulation factor, developmental toxicity and mutagenicity of SMX and of its degradation products were speculated (Fig. 9). The acute toxicity of SMX on the Daphnia magna (LC50, is the concentration at which a chemical will kill 50% of laboratory animals exposed to it under proper testing conditions after 48 h.) was 16.28 mg L^{-1}, which was classified as "toxic". However, the toxicity of the degradation products treated by Cu-Fe^{vac}-LDH/PMS process decreased significantly, and even some products reached non-toxic levels. At the same time, there has also been an increase in acute toxicity of individual products (P3). From the overall

perspective of bioaccumulation factors and mutagenicity, the toxicity of the degradation products to organisms was reduced. In addition, the mutagenicity of SMX was negative, and its products showed a downward trend except for P2. In terms of developmental toxicity, about half of the degradation products have increased developmental toxicity. Overall, although the Cu-Fe^{vac}-LDH/PMS process can achieve low-toxicity treatment of SMX, most of the products still have certain toxic hazards, and subsequent wastewater treatment still needs attention and is expected to achieve non-toxic and safe treatment.

4. Conclusions

Oxidative efficacy of high-valent iron-oxo species, i.e., Fe$^{(IV)}$=O or Fe$^{(V)}$=O, showed great potential advantages for their practical application in wastewater treatment. However, it is not affordable and practical to gain Fe$^{(IV)}$=O or Fe$^{(V)}$=O species from reduction of ferrate, which is required to be produced from Fe(II) or Fe(III) in advance [47]. The current study offered an idea methodology for direct conversion of naturally abundant Fe(II) and Fe(III) into high-valent iron-oxo species of Fe$^{(IV)}$=O and Fe$^{(V)}$=O theoretically by introducing defect engineering in cationic vacancies along with PMS oxidation. Regarding degradation efficiency of high-valent iron-oxo species for SMX and their applications in broad ranges of pH environments and real water matrix, such technique would have wide application perspectives. Further study is encouraged to focus on physical and chemical stability of high-valent iron-oxo species, potential confounding variables during the reactions, and their oxidative performance in actual wastewater treatments.

CRediT authorship contribution statement

Xiaoyue Zhou: Conceptualization, Methodology, Formal analysis, Investigation, Data curation, Writing – original draft, Writing – review & editing. **Jieqiong Kang:** Methodology, Formal analysis. **Zhenjie Li:** Data curation. **Yanan Pan:** Investigation. **Jieyun Bai:** Copyright of calculation software. **Rongliang Qiu:** Review and provide advice. **Renli Yin** & **Adela Jing Li:** Project administration, Funding acquisition, Resources, Conceptualization, Writing – review & editing.

Declaration of Competing Interest

The authors declare that they have no known competing financial interests or personal relationships that could have appeared to influence the work reported in this paper.

Data availability

Data will be made available on request.

Acknowledgements

Appendix A. Supporting information

Detailed information on material characterization (e.g., SEM), organic and inorganic ion concentration measurements, energy consumption calculations; active species detection (e.g., EPR) (PDF). Supplementary data associated with this article can be found in the online version at doi:10.1016/j.apcatb.2023.122640.

References

[1] J. Qu, Y. Xu, X. Zhang, M. Sun, Y. Tao, X. Zhang, G. Zhang, C. Ge, Y. Zhang, Ball milling-assisted preparation of N-doped biochar loaded with ferrous sulfide as persulfate activator for phenol degradation: multiple active sites-triggered radical/non-radical mechanism, Appl. Catal. B Environ. 316 (2022) 121639, https://doi.org/10.1016/j.apcatb.2022.121639.

[2] R. Yin, B. Jing, S. He, J. Hu, G. Lu, Z. Ao, C. Wang, M. Zhu, Near-infrared light to heat conversion in peroxydisulfate activation with MoS2: a new photo-activation process for water treatment, Water Res. 190 (2021) 116720, https://doi.org/10.1016/j.watres.2020.116720.

[3] Z. Xiao, X. Feng, H. Shi, B. Zhou, W. Wang, N. Ren, Why the cooperation of radical and non-radical pathways in PMS system leads to a higher efficiency than a single pathway in tetracycline degradation, J. Hazard. Mater. 424 (2022) 127247, https://doi.org/10.1016/j.jhazmat.2021.127247.

[4] B.D. Yirsaw, M. Megharaj, Z. Chen, R. Naidu, Environmental application and ecological significance of nano-zero valent iron, J. Environ. Sci. 44 (2016) 88–98, https://doi.org/10.1016/j.jes.2015.07.016.

[5] Z. He, X. Huang, Q. Chen, C. Zhai, Y. Hu, M. Zhu, Pt nanoclusters embedded Fe-based metal-organic framework as a dual-functional electrocatalyst for hydrogen evolution and alcohols oxidation, J. Colloid Interface Sci. 616 (2022) 279–286, https://doi.org/10.1016/j.jcis.2022.02.073.

[6] Q. Wang, N. Zhu, E. Liu, C. Zhang, J.C. Crittenden, Y. Zhang, Y. Cong, Fabrication of visible-light active Fe2O3-GQDs/NF-TiO2 composite film with highly enhanced photoelectrocatalytic performance, Appl. Catal. B Environ. 205 (2017) 347–356, https://doi.org/10.1016/j.apcatb.2016.11.046.

[7] W. Oh, Z. Dong, T. Lim, Generation of sulfate radical through heterogeneous catalysis for organic contaminants removal: current development, challenges and prospects, Appl. Catal. B Environ. 194 (2016) 169–201, https://doi.org/10.1016/j.apcatb.2016.04.003.

[8] J. Zou, J. Ma, L. Chen, X. Li, Y. Guan, P. Xie, C. Pan, Rapid acceleration of ferrous iron/peroxymonosulfate oxidation of organic pollutants by promoting Fe(III)/Fe (II) cycle with hydroxylamine, Environ. Sci. Technol. 47 (2013) 11685–11691, https://doi.org/10.1021/es4019145.

[9] Z. Wang, W. Qiu, S. Pang, Q. Guo, C. Guan, J. Jiang, Aqueous Iron(IV)-oxo complex: an emerging powerful reactive oxidant formed by iron(II)-based advanced oxidation processes for oxidative water treatment, Environ. Sci. Technol. 56 (2022) 1492–1509, https://doi.org/10.1021/acs.est.1c04530.

[10] X. Cheng, H. Liang, A. Ding, X. Tang, B. Liu, X. Zhu, Z. Gan, D. Wu, G. Li, Ferrous iron/peroxymonosulfate oxidation as a pretreatment for ceramic ultrafiltration membrane: control of natural organic matter fouling and degradation of atrazine, Water Res. 113 (2017) 32–41, https://doi.org/10.1016/j.watres.2017.01.055.

[11] Y. Bao, Y. Lian, K. Huang, H. Yu, W. Liu, J. Zhang, M. Xing, Generating high-valent iron-oxo =FeIV=O complexes in neutral microenvironments through peroxymonosulfate activation by Zn–Fe layered double hydroxides, Angew. Chem. Int. Ed. 134 (2022) 1–10, https://doi.org/10.1002/ange.202209542.

[12] Y. Zheng, Y. Luo, Q. Ruan, S. Wang, J. Yu, X. Guo, W. Zhang, H. Xie, Z. Zhang, Y. Huang, Plasma-induced hierarchical amorphous carbon nitride nanostructure with two N2C-site vacancies for photocatalytic H2O2 production, Appl. Catal. B Environ. 311 (2022), 121372, https://doi.org/10.1016/j.apcatb.2022.121372.

[13] L. Jin, S. You, N. Ren, B. Ding, Y. Liu, Mo vacancy-mediated activation of peroxymonosulfate for ultrafast micropollutant removal using an electrified mxene filter functionalized with Fe single atoms, Environ. Sci. Technol. 56 (2022) 11750–11759, https://doi.org/10.1021/acs.est.2c03904.

[14] L. Wu, P. Guo, X. Wang, H. Li, X. Zhang, K. Chen, P. Zhou, The synergy of sulfur vacancies and heterostructure on CoS@FeS nanosheets for boosting the peroxymonosulfate activation, Chem. Eng. J. 446 (2022) 136759, https://doi.org/10.1016/j.cej.2022.136759.

[15] Y. Rao, Y. Zhang, J. Fan, G. Wei, D. Wang, F. Han, Y. Huang, J. Croue, Enhanced peroxymonosulfate activation by Cu-doped LaFeO3 with rich oxygen vacancies: compound-specific mechanisms, Chem. Eng. J. 435 (2022), 134882, https://doi.org/10.1016/j.cej.2022.134882.

[16] J. Jiang, Z. Zhao, J. Gao, T. Li, M. Li, D. Zhou, S. Dong, Nitrogen vacancy-modulated peroxymonosulfate nonradical activation for organic contaminant removal via high-valent cobalt-oxo species, Environ. Sci. Technol. 56 (2022) 5611–5619, https://doi.org/10.1021/acs.est.2c01913.

[17] Y. Yu, H. Chen, L. Yan, C. Jing, Oxygen vacancy modulated interface chemistry: identifying iron(IV) in heterogeneous Fenton reaction, Environ. Sci. Nano 8 (2021) 978–985, https://doi.org/10.1039/d0en01213k.

[18] Y. Yang, W. Si, Y. Peng, Y. Wang, H. Liu, Z. Su, J. Li, Defect engineering on CuMn2O4 spinel surface: a new path to high-performance oxidation catalysts, Environ. Sci. Technol. (2022) 16249–16258, https://doi.org/10.1021/acs.est.2c04858.

[19] B. Liu, Y. Wang, H.Q. Peng, R. Yang, Z. Jiang, X. Zhou, C.S. Lee, H. Zhao, W. Zhang, Iron vacancies induced bifunctionality in ultrathin feroxyhyte nanosheets for overall water splitting, Adv. Mater. 30 (2018), e1803144, https://doi.org/10.1002/adma.201803144.

[20] L. Peng, N. Yang, Y. Yang, Q. Wang, X. Xie, D. Sun-Waterhouse, L. Shang, T. Zhang, G.I.N. Waterhouse, Atomic cation-vacancy engineering of NiFe-Layered double hydroxides for improved activity and stability towards the oxygen evolution reaction, Angew. Chem. Int. Ed. 60 (2021) 24612–24619, https://doi.org/10.1002/anie.202109938.

[21] M. Xia, T. Liu, N. Peng, R. Zheng, X. Cheng, H. Zhu, H. Yu, M. Shui, J. Shu, Lab-scale in situ x-ray diffraction technique for different battery systems: designs, applications, and perspectives, Small Methods 3 (2019), 1900119, https://doi.org/10.1002/smtd.201900119.

[22] Y. Ma, F. Chen, Q. Yang, Y. Zhong, X. Shu, F. Yao, T. Xie, X. Li, D. Wang, G. Zeng, Sulfate radical induced degradation of methyl violet azo dye with CuFe layered doubled hydroxide as heterogeneous photoactivator of persulfate, J. Environ. Manag. 227 (2018) 406–414, https://doi.org/10.1016/j.jenvman.2018.08.030.

[23] R. Yin, Y. Chen, J. Hu, S. Jin, W. Guo, M. Zhu, Peroxydisulfate bridged photocatalysis of covalent triazine framework for carbamazepine degradation, Chem. Eng. J. 427 (2022), 131613, https://doi.org/10.1016/j.cej.2021.131613.

[24] S. Wang, J. Zhu, T. Li, F. Ge, Z. Zhang, R. Zhu, H. Xie, Y. Xu, Oxygen vacancy-mediated CuCoFe/tartrate-LDH catalyst directly activates oxygen to produce superoxide radicals: transformation of active species and implication for nitrobenzene degradation, Environ. Sci. Technol. 56 (2022) 7924–7934, https://doi.org/10.1021/acs.est.2c00522.

[25] S. He, R. Yin, Y. Chen, T. Lai, W. Guo, L. Zeng, M. Zhu, Consolidated 3D Co3Mn-layered double hydroxide aerogel for photo-assisted peroxymonosulfate activation in metronidazole degradation, Chem. Eng. J. 423 (2021), 130172, https://doi.org/10.1016/j.cej.2021.130172.

[26] Y. Fu, M. Tan, Z. Guo, D. Hao, Y. Xu, H. Du, C. Zhang, J. Guo, Q. Li, Q. Wang, Fabrication of wide-spectra-responsive NA/NH2-MIL-125(Ti) with boosted activity for Cr(VI) reduction and antibacterial effects, Chem. Eng. J. 452 (2023), 139417, https://doi.org/10.1016/j.cej.2022.139417.

[27] J. Guo, D. Ma, F. Sun, G. Zhuang, Q. Wang, A.M. Al-Enizi, A. Nafady, S. Ma, Substituent engineering in g-C3N4/COF heterojunctions for rapid charge separation and high photo-redox activity, Sci. China-Chem. 65 (2022) 1704–1709. https://doi.org/10.1007/s11426-022-1350-1.

[28] R. Yin, Y. Chen, J. Hu, G. Lu, L. Zeng, W. Choi, M. Zhu, Complexes of Fe(III)-organic pollutants that directly activate Fenton-like processes under visible light, Appl. Catal. B Environ. 283 (2021), 119663, https://doi.org/10.1016/j.apcatb.2020.119663.

[29] Y. Fu, K. Zhang, Y. Zhang, Y. Cong, Q. Wang, Fabrication of visible-light-active MR/NH2-MIL-125(Ti) homojunction with boosted photocatalytic performance, Chem. Eng. J. 412 (2021), 128722, https://doi.org/10.1016/j.cej.2021.128722.

[30] Z. Wang, W. Qiu, S. Pang, J. Jiang, Effect of chelators on the production and nature of the reactive intermediates formed in Fe(II) activated peroxydisulfate and hydrogen peroxide processes, Water Res. 164 (2019), 114957, https://doi.org/10.1016/j.watres.2019.114957.

[31] H. Wang, S. Wang, Y. Liu, J. Fu, P. Wu, G. Zhou, Degradation of diclofenac by Fe(II)-activated bisulfite: kinetics, mechanism and transformation products, Chemosphere 237 (2019), 124518, https://doi.org/10.1016/j.chemosphere.2019.124518.

[32] H. Li, N. Yuan, J. Qian, B. Pan, Mn2O3 as an electron shuttle between peroxymonosulfate and organic pollutants: the dominant role of surface reactive Mn(IV) species, Environ. Sci. Technol. 56 (2022) 4498–4506, https://doi.org/10.1021/acs.est.1c08790.

[33] J. Huang, Y. Dai, K. Singewald, C. Liu, S. Saxena, H. Zhang, Effects of MnO2 of different structures on activation of peroxymonosulfate for bisphenol A degradation under acidic conditions, Chem. Eng. J. 370 (2019) 906–915, https://doi.org/10.1016/j.cej.2019.03.238.

[34] R. Yin, W. Guo, N. Ren, L. Zeng, M. Zhu, New insight into the substituents affecting the peroxydisulfate nonradical oxidation of sulfonamides in water, Water Res. 171 (2020), 115374, https://doi.org/10.1016/j.watres.2019.115374.

[35] X. Chen, W. Oh, Z. Hu, Y. Sun, R.D. Webster, S. Li, T. Lim, Enhancing sulfacetamide degradation by peroxymonosulfate activation with N-doped graphene produced through delicately-controlled nitrogen functionalization via tweaking thermal annealing processes, Appl. Catal. B Environ. 225 (2018) 243–257, https://doi.org/10.1016/j.apcatb.2017.11.071.

[36] Y. Ahn, E. Yun, J. Seo, C. Lee, S.H. Kim, J. Kim, J. Lee, Activation of peroxymonosulfate by surface-loaded noble metal nanoparticles for oxidative degradation of organic compounds, Environ. Sci. Technol. 50 (2016) 10187–10197, https://doi.org/10.1021/acs.est.6b02841.

[37] L. Wang, W. Lu, D. Ni, T. Xu, N. Li, Z. Zhu, H. Chen, W. Chen, Solar-initiated photocatalytic degradation of carbamazepine on excited-state hexadecachlorophthalocyanine in the presence of peroxymonosulfate, Chem. Eng. J. 330 (2017) 625–634, https://doi.org/10.1016/j.cej.2017.07.172.

[38] S. Mondal, Y. Hangun-Balkir, L. Alexandrova, D. Link, B. Howard, P. Zandhuis, A. Cugini, C.P. Horwitz, T.J. Collins, Oxidation of sulfur components in diesel fuel using Fe-TAML (R) catalysts and hydrogen peroxide, Catal. Today 116 (2006) 554–561, https://doi.org/10.1016/j.cattod.2006.06.025.

[39] L. Luo, Z. Wang, Q. Guo, X. Wei, J. Hu, Y. Luo, J. Jiang, Evidence for the involvement of Fe(IV) in water treatment by Fe(III)-activated sulfite, Environ. Chem. Lett. 20 (2022) 91–99, https://doi.org/10.1007/s10311-021-01324-6.

[40] Z. Wang, W. Qiu, S. Pang, Y. Gao, Y. Zhou, Y. Cao, J. Jiang, Relative contribution of ferryl ion species (Fe(IV)) and sulfate radical formed in nanoscale zero valent iron activated peroxydisulfate and peroxymonosulfate processes, Water Res. 172 (2020), 115504, https://doi.org/10.1016/j.watres.2020.115504.

[41] N. Jiang, H. Xu, L. Wang, J. Jiang, T. Zhang, Nonradical oxidation of pollutants with single-atom-Fe(III)-activated persulfate: Fe(V) being the possible intermediate oxidant, Environ. Sci. Technol. 54 (2020) 14057–14065, https://doi.org/10.1021/acs.est.0c04867.

[42] M. Luo, H. Zhou, P. Zhou, L. Lai, W. Liu, Z. Ao, G. Yao, H. Zhang, B. Lai, Insights into the role of in-situ and ex-situ hydrogen peroxide for enhanced ferrate(VI) towards oxidation of organic contaminants, Water Res. 203 (2021), 117548, https://doi.org/10.1016/j.watres.2021.117548.

[43] S. Wang, Y. Deng, B. Shao, J. Zhu, Z. Hu, X. Guan, Three kinetic patterns for the oxidation of emerging organic contaminants by Fe(VI): the critical roles of Fe(V) and Fe(IV), Environ. Sci. Technol. 55 (2021) 11338–11347, https://doi.org/10.1021/acs.est.1c03813.

[44] R. Yin, W. Guo, N. Ren, L. Zeng, M. Zhu, New insight into the substituents affecting the peroxydisulfate nonradical oxidation of sulfonamides in water, Water Res. 171 (2020), 115374, https://doi.org/10.1016/j.watres.2019.115374.

[45] Y. Lee, R. Kissner, U. von Gunten, Reaction of ferrate(VI) with ABTS and self-decay of ferrate(VI): kinetics and mechanisms, Environ. Sci. Technol. 48 (2014) 5154–5162, https://doi.org/10.1021/es500804g.

[46] S. Sun, J. Jiang, L. Qiu, S. Pang, J. Li, C. Liu, L. Wang, M. Xue, J. Ma, Activation of ferrate by carbon nanotube for enhanced degradation of bromophenols: kinetics, products, and involvement of Fe(V)/Fe(IV), Water Res. 156 (2019) 1–8, https://doi.org/10.1016/j.watres.2019.02.057.

[47] V.K. Sharma, Ferrate(VI) and ferrate(V) oxidation of organic compounds: kinetics and mechanism, Coord. Chem. Rev. 257 (2013) 495–510, https://doi.org/10.1016/j.ccr.2012.04.014.